

Recursive regularised lattice Boltzmann method for magnetohydrodynamics

Alessandro De Rosis¹

Department of Mechanical and Aerospace Engineering, The University of Manchester, Manchester M13 9PL, United Kingdom

(Dated: 17 February 2026)

We present and test a recursive regularised lattice Boltzmann method for incompressible magnetohydrodynamic (MHD) flows. The approach is based on a double-distribution formulation, in which the magnetic field is evolved using a standard BGK lattice Boltzmann scheme, while the fluid solver is enhanced through a Hermite-based recursive regularisation of the non-equilibrium moments. The method exploits a fourth-order Hermite expansion of the equilibrium distribution on the D2Q9 lattice, allowing higher-order isotropy to be retained while selectively filtering spurious non-hydrodynamic contributions. The regularisation procedure reconstructs the non-equilibrium distribution from physically consistent Hermite coefficients, avoiding explicit evaluation of velocity gradients. The resulting scheme preserves the correct incompressible MHD limit, improves numerical stability at low viscosities, and reduces lattice-dependent artefacts. The proposed formulation provides a robust and versatile framework for MHD simulations and offers a systematic route for extending regularised lattice Boltzmann methods to coupled multiphysics systems.

I. INTRODUCTION

Magnetohydrodynamics (MHD) governs the coupled dynamics of electrically conducting fluids and magnetic fields and is central to a wide range of physical and technological applications, including plasma physics, astrophysical and geophysical flows, liquid-metal technologies, and electromagnetic flow control¹. From a modelling standpoint, the incompressible resistive MHD flow is described by the coupled system

$$\partial_t \mathbf{u} + \mathbf{u} \cdot \nabla \mathbf{u} = -\frac{\nabla p}{\rho_0} + \nu \nabla^2 \mathbf{u} + \frac{(\nabla \times \mathbf{b}) \times \mathbf{b}}{\rho_0}, \quad (1)$$

$$\partial_t \mathbf{b} + \mathbf{u} \cdot \nabla \mathbf{b} = \mathbf{b} \cdot \nabla \mathbf{u} + \eta \nabla^2 \mathbf{b}, \quad (2)$$

supplemented by the solenoidal constraints

$$\nabla \cdot \mathbf{u} = 0, \quad \nabla \cdot \mathbf{b} = 0. \quad (3)$$

Here ∂_t denotes the partial derivative with respect to time t , ∇ is the gradient operator, \mathbf{u} and \mathbf{b} denote the velocity and magnetic fields, respectively, p is the hydrodynamic pressure, ν is the kinematic viscosity, η is magnetic diffusivity, and ρ_0 is the reference fluid mass density. The numerical prediction of MHD flows is particularly challenging due to the strong non-linear coupling between velocity and magnetic fields, the coexistence of multiple transport mechanisms, and the requirement to satisfy solenoidal constraints on both fields². These difficulties are especially pronounced in regimes characterised by low viscosity, low magnetic diffusivity, or strong Lorentz forces, where numerical dissipation and spurious artefacts can significantly affect solution fidelity^{3,4}.

The lattice Boltzmann method⁵ (LBM) has emerged as an attractive mesoscopic alternative to conventional discretisations of the incompressible MHD equations. Briefly, the flow physics arises from the evolution of collections (also known as distributions or populations) of fictitious particles colliding and streaming along

the links of a fixed Cartesian lattice. The earliest attempt to construct a lattice gas automaton for magnetohydrodynamics dates back to the work of Montgomery & Doolen⁶. Their formulation is based on a magnetic vector potential approach, in which the Lorentz force is incorporated through the evaluation of a Laplacian operator. This requires the introduction of an additional non-local finite-difference procedure. Subsequently, Chen *et al.*⁷ proposed a purely local lattice gas model. However, this approach requires solving a 36-state MHD cellular automaton at each node of a two-dimensional hexagonal lattice, resulting in a prohibitively high computational cost. Martinez *et al.*⁸ later reduced the number of states to 12, partially mitigating this limitation.

An alternative strategy was introduced by Succi *et al.*⁹ who developed a hybrid scheme coupling the lattice Boltzmann method with a finite-difference discretisation for two-dimensional MHD flows. While computationally efficient, this formulation restricts the magnetic Prandtl number,

$$\text{Pr}_m = \frac{\nu}{\eta}, \quad (4)$$

to unity.

A major advance was achieved by Dellar¹⁰ who demonstrated that the MHD equations can be recovered from two coupled lattice Boltzmann equations (LBEs) based on the single-relaxation-time Bhatnagar–Gross–Krook (BGK) collision operator¹¹. The first LBE evolves scalar populations f_i of fictitious particles carrying mass, from which the fluid density ρ and momentum $\rho \mathbf{u}$ are obtained. The second LBE governs vector-valued populations \mathbf{g}_j that describe the evolution of the magnetic field \mathbf{b} . This formulation overcomes the principal limitations of previous approaches: it is fully local, allows for arbitrary magnetic Prandtl numbers, and remains computationally efficient. In the present work, this scheme is adopted as a baseline

and extended to develop an improved method tailored to high-Reynolds-number MHD flows.

The numerical properties of lattice Boltzmann MHD models depend strongly on the choice of collision operator. While the BGK model remains widely used due to its simplicity and efficiency, it is well known to suffer from limited numerical stability at low viscosities and from sensitivity to lattice non-hydrodynamic modes¹². In magnetohydrodynamic flows, these limitations are amplified by the Lorentz force and by the transfer of energy across multiple spatial scales¹³.

To address these issues, several advanced collision models have been proposed. Multiple-relaxation-time (MRT) formulations based on raw moments (RMs) improve stability by relaxing different kinetic moments at distinct rates^{14,15}, while lattice Boltzmann methods based on central moments (CMs) and cumulants further enhance robustness by performing the collision process in a locally comoving frame, improving Galilean invariance and isotropy^{16,17}. Central-moment formulations have been successfully applied to a wide range of challenging flow problems, including multiphysics and magnetohydrodynamic systems, demonstrating excellent stability and accuracy^{18–20}.

An alternative stabilisation strategy is provided by regularised lattice Boltzmann methods, in which the non-equilibrium distribution is reconstructed from a truncated Hermite expansion²¹. More recently, recursive regularisation (RR) techniques have been proposed to systematically reconstruct higher-order non-equilibrium moments from lower-order information, leading to improved isotropy and robustness in hydrodynamic flows^{22,23}. Despite these advances, including extensions to multiphase flows²⁴, recursive regularisation has not yet been systematically explored in the context of magnetohydrodynamic lattice Boltzmann models. Existing work on its application to MHD remains limited in scope and does not provide a comprehensive assessment²⁵. The present study fills this gap by offering the first systematic investigation of the method for MHD flows, rigorously assessing accuracy, stability, and scalability over a wide range of regimes. Indeed, we aim to assess whether the stabilisation and isotropy benefits of recursive regularisation observed in hydrodynamic flows carry over to magnetohydrodynamic systems.

To this end, we propose a recursive regularised lattice Boltzmann method for incompressible two-dimensional MHD flows and explicitly contrast its performance with that of three distinct collision models: BGK, MRT and CMs-based LBMs. We adopt a hybrid double-distribution strategy in which the magnetic field is evolved using the BGK scheme proposed by Dellar¹⁰, while the fluid solver is enhanced through recursive regularisation of the non-equilibrium moments. The approach is based on a fourth-order Hermite expansion of the equilibrium distribution on the D2Q9 lattice and avoids the explicit evaluation of velocity gradients.

The method is validated using the Orszag–Tang

vortex, a canonical benchmark for non-linear MHD dynamics featuring strong velocity–magnetic field coupling, current-sheet formation, and a transition toward MHD turbulence²⁶. The impact of regularisation on numerical stability, dissipation, and the accurate capture of key MHD features are assessed.

The paper is organised as follows. Section II recalls the BGK lattice Boltzmann formulation and presents our recursive regularisation procedure. Numerical results for the Orszag–Tang vortex at low and high Reynolds numbers are presented in Section III, followed by concluding remarks in Section IV.

II. METHODOLOGY

We consider a two-dimensional Cartesian domain with coordinates (x, y) , filled with an electrically conducting fluid of reference mass density ρ_0 , kinematic viscosity ν , and magnetic diffusivity η . Here the gradient operator is $\nabla = [\partial_x, \partial_y]$, and the flow velocity and magnetic field vectors are $\mathbf{u} = [u_x, u_y]$ and $\mathbf{b} = [b_x, b_y]$, respectively. In the remainder of this section, we first briefly recall the BGK lattice Boltzmann formulation for MHD and subsequently introduce our strategy based on recursive regularisation.

A. BGK lattice Boltzmann formulation

Following Dellar¹⁰, the magnetohydrodynamic equations are solved using a double-distribution-function LBM. The fluid dynamics are described by a scalar particle distribution function $f_i(\mathbf{x}, t)$ defined on a D2Q9 lattice, where the index $i = 0, \dots, 8$ labels the discrete velocity directions $\mathbf{c}_i = [c_{i,x}, c_{i,y}]$, given by²⁷

$$c_{i,x} = [0, -1, -1, -1, 0, 1, 1, 1, 0], \quad (5)$$

$$c_{i,y} = [0, 1, 0, -1, -1, -1, 0, 1, 1]. \quad (6)$$

\mathbf{x} denotes the spatial location of a given lattice point. The magnetic field is evolved using auxiliary vector-valued distribution functions $\mathbf{g}_j = [g_{j,x}, g_{j,y}]$ defined on a D2Q5 lattice, where $j = 0, \dots, 4$ and the corresponding lattice velocities $\mathbf{e}_j = [e_{j,x}, e_{j,y}]$ are

$$e_{j,x} = [0, -1, 0, 1, 0], \quad e_{j,y} = [0, 0, -1, 0, 1]. \quad (7)$$

Within the BGK approximation, the LBEs read as follows

$$f_i(\mathbf{x} + \mathbf{c}_i \Delta t, t + \Delta t) = f_i^*(\mathbf{x}, t), \quad (8)$$

$$\mathbf{g}_j(\mathbf{x} + \mathbf{e}_j \Delta t, t + \Delta t) = \mathbf{g}_j^*(\mathbf{x}, t), \quad (9)$$

where $\Delta t = 1$ is the lattice time step and the so-called post-collision populations (denoted by the superscript $*$) are evaluated as

$$f_i^*(\mathbf{x}, t) = f_i^{\text{eq}}(\mathbf{x}, t) + (1 - \omega) f_i^{\text{neq}}(\mathbf{x}, t), \quad (10)$$

$$\mathbf{g}_j^*(\mathbf{x}, t) = \mathbf{g}_j^{\text{eq}}(\mathbf{x}, t) + (1 - \omega_m) \mathbf{g}_j^{\text{neq}}(\mathbf{x}, t). \quad (11)$$

The relaxation frequencies ω and ω_m are related to the kinematic viscosity ν and magnetic diffusivity η through

$$\nu = \left(\frac{1}{\omega} - \frac{1}{2} \right), \quad \eta = \left(\frac{1}{\omega_m} - \frac{1}{2} \right), \quad (12)$$

respectively. To lighten the notation, the dependence on space and time is implicitly assumed in the following. The equilibrium distribution functions are given by

$$f_i^{\text{eq}} = w_i \rho \left[1 + \frac{\mathcal{H}_i^{(1)} \cdot \mathbf{u}}{c_s^2} + \frac{1}{2c_s^4} \mathcal{H}_i^{(2)} : \mathbf{u} \mathbf{u} \right] + \frac{w_i}{2c_s^4} \left[\frac{1}{2} |\mathbf{b}|^2 |\mathbf{c}_i|^2 - (\mathbf{c}_i \cdot \mathbf{b})^2 \right], \quad (13)$$

$$\mathbf{g}_{j,\alpha}^{\text{eq}} = \psi_j \left[b_\alpha + \frac{e_{j,\beta}}{c_s^2} (u_\beta b_\alpha - u_\alpha b_\beta) \right], \quad (14)$$

where $c_s = 1/\sqrt{3}$ is the lattice sound speed. The weighting factors for the velocity field are

$$w_0 = \frac{4}{9}, \quad w_{1,3,5,7} = \frac{1}{36}, \quad w_{2,4,6,8} = \frac{1}{9}, \quad (15)$$

while for the magnetic field

$$\psi_0 = \frac{1}{3}, \quad \psi_{1,2,3,4} = \frac{1}{6}. \quad (16)$$

The non-equilibrium terms are simply computed as

$$f_i^{\text{neq}} = f_i - f_i^{\text{eq}}, \quad (17)$$

$$\mathbf{g}_j^{\text{neq}} = \mathbf{g}_j - \mathbf{g}_j^{\text{eq}}. \quad (18)$$

Rather than using the second-order equilibrium (13), we follow the approach of Malaspinas²¹ and Coreixas *et al.*²², who showed that the full isotropy of the D2Q9 lattice can be exploited by expanding the equilibrium distribution in a Hermite basis up to fourth order. The resulting equilibrium reads

$$f_i^{\text{eq}} = w_i \rho \left[\underbrace{1}_{\mathcal{O}(\mathbf{u}^0)} + \underbrace{\frac{\mathcal{H}_i^{(1)} \cdot \mathbf{u}}{c_s^2}}_{\mathcal{O}(\mathbf{u}^1)} + \underbrace{\frac{1}{2c_s^4} \mathcal{H}_i^{(2)} : \mathbf{u} \mathbf{u}}_{\mathcal{O}(\mathbf{u}^2)} + \underbrace{\frac{1}{2c_s^6} \left(\mathcal{H}_{i,xy}^{(3)} u_x^2 u_y + \mathcal{H}_{i,xyy}^{(3)} u_x u_y^2 \right)}_{\mathcal{O}(\mathbf{u}^3)} + \underbrace{\mathcal{H}_{i,xyy}^{(4)} u_x^2 u_y^2}_{\mathcal{O}(\mathbf{u}^4)} + \underbrace{\frac{w_i}{2c_s^4} \left[\frac{1}{2} |\mathbf{b}|^2 |\mathbf{c}_i|^2 - (\mathbf{c}_i \cdot \mathbf{b})^2 \right]}_{\text{Maxwell stress } \mathcal{O}(\mathbf{b}^2)} \right]. \quad (19)$$

The Hermite tensors are defined as

$$\mathcal{H}_i^{(0)} = 1,$$

$$\begin{aligned} \mathcal{H}_{i,\alpha}^{(1)} &= c_{i,\alpha}, \\ \mathcal{H}_{i,\alpha\beta}^{(2)} &= c_{i,\alpha} c_{i,\beta} - c_s^2 \delta_{\alpha\beta}, \\ \mathcal{H}_{i,\alpha\beta\gamma}^{(3)} &= c_{i,\alpha} c_{i,\beta} c_{i,\gamma} - c_s^2 (c_{i,\alpha} \delta_{\beta\gamma} + c_{i,\beta} \delta_{\alpha\gamma} + c_{i,\gamma} \delta_{\alpha\beta}), \\ \mathcal{H}_{i,\alpha\beta\gamma\delta}^{(4)} &= c_{i,\alpha} c_{i,\beta} c_{i,\gamma} c_{i,\delta} - c_s^2 \sum_{\text{perm}} c_{i,\alpha} c_{i,\beta} \delta_{\gamma\delta} + \\ &\quad c_s^4 \sum_{\text{perm}} \delta_{\alpha\beta} \delta_{\gamma\delta}, \end{aligned} \quad (20)$$

where $\delta_{\alpha\beta}$ is the Kronecker delta and $(\alpha, \beta, \gamma, \delta) \in \{x, y\}^4$. The equilibrium distribution f_i^{eq} is fixed throughout this study to the fourth-order Hermite formulation given in Eq. (19).

Finally, the macroscopic fields are obtained as

$$\rho = \sum_i f_i, \quad \mathbf{u} = \frac{\sum_i f_i \mathbf{c}_i}{\rho}, \quad \mathbf{b} = \sum_j \mathbf{g}_j. \quad (21)$$

It is worth noting that the LBM allows us to compute the electric current $j_z = \nabla \times \mathbf{b}$ locally from the populations as²⁸

$$j_z = -\frac{\omega_m}{c_s^2} \varepsilon_{\alpha\beta} \sum_j (e_{j,\alpha} g_{j,\beta} - e_{j,\beta} g_{j,\alpha}^{\text{eq}}), \quad (22)$$

where

$$\sum_j e_{j,\alpha} g_{j,\beta}^{\text{eq}} = u_\beta b_\alpha - u_\alpha b_\beta, \quad (23)$$

and $\varepsilon_{\alpha\beta}$ is the Levi-Civita permutation tensor, without the need to evaluate non-local finite-difference operators.

B. Recursive regularised lattice Boltzmann method

We now derive a recursive regularisation strategy for magnetohydrodynamic flows. Specifically, we adopt a hybrid approach in which the magnetic field is evolved using the standard BGK lattice Boltzmann scheme described above, while a dedicated regularisation procedure is applied to the fluid solver in order to enhance numerical stability and accuracy.

Following Coreixas *et al.*²², we can express the post-collision state f_i^* in terms of a truncated Hermite expansion as

$$f_i^* = w_i \sum_{n=0}^4 \frac{1}{n! c_s^{2n}} \left[\mathbf{a}_0^{(n)} + (1 - \omega) \mathbf{a}_1^{(n)} \right] : \mathcal{H}_i^{(n)}. \quad (24)$$

The equilibrium Hermite coefficients $\mathbf{a}_0^{(n)}$ are given by

$$\begin{aligned} \mathbf{a}_0^{(0)} &= \rho, \\ \mathbf{a}_{0,\alpha}^{(1)} &= \rho u_\alpha, \\ \mathbf{a}_{0,\alpha\beta}^{(2)} &= \rho u_\alpha u_\beta + M_{\alpha\beta}, \\ \mathbf{a}_{0,\alpha\beta\gamma}^{(3)} &= \rho u_\alpha u_\beta u_\gamma + u_\alpha M_{\beta\gamma} + u_\beta M_{\alpha\gamma} + u_\gamma M_{\alpha\beta}, \end{aligned}$$

$$a_{0,\alpha\beta\gamma\delta}^{(4)} = \rho u_\alpha u_\beta u_\gamma u_\delta + \left(u_\alpha u_\beta M_{\gamma\delta} + u_\alpha u_\gamma M_{\beta\delta} + u_\alpha u_\delta M_{\beta\gamma} + u_\beta u_\gamma M_{\alpha\delta} + u_\beta u_\delta M_{\alpha\gamma} + u_\gamma u_\delta M_{\alpha\beta} \right), \quad (25)$$

where the Maxwell stress tensor is defined as¹⁰

$$M_{\alpha\beta} = \frac{1}{2} |\mathbf{b}|^2 \delta_{\alpha\beta} - b_\alpha b_\beta. \quad (26)$$

When the magnetic field is neglected, Eqs. (25) reduce exactly to the pure hydrodynamic formulation²².

The corresponding non-equilibrium Hermite coefficients $\mathbf{a}_1^{(n)}$ read

$$\begin{aligned} a_1^{(0)} &= 0, \\ a_{1,\alpha}^{(1)} &= 0, \\ a_{1,\alpha\beta}^{(2)} &= -\nu \rho c_s^2 [\partial_\alpha u_\beta + \partial_\beta u_\alpha - (\partial_\gamma u_\gamma) \delta_{\alpha\beta}], \\ a_{1,\alpha\beta\gamma}^{(3)} &= u_\alpha a_{1,\beta\gamma}^{(2)} + u_\beta a_{1,\alpha\gamma}^{(2)} + u_\gamma a_{1,\alpha\beta}^{(2)}, \\ a_{1,\alpha\beta\gamma\delta}^{(4)} &= u_\alpha a_{1,\beta\gamma\delta}^{(3)} + u_\beta a_{1,\alpha\gamma\delta}^{(3)} + u_\gamma a_{1,\alpha\beta\delta}^{(3)} + u_\delta a_{1,\alpha\beta\gamma}^{(3)} - \\ &\quad [u_\alpha u_\beta a_{1,\gamma\delta}^{(2)} + u_\alpha u_\gamma a_{1,\beta\delta}^{(2)} + u_\alpha u_\delta a_{1,\beta\gamma}^{(2)} + \\ &\quad u_\beta u_\gamma a_{1,\alpha\delta}^{(2)} + u_\beta u_\delta a_{1,\alpha\gamma}^{(2)} + u_\gamma u_\delta a_{1,\alpha\beta}^{(2)}]. \end{aligned} \quad (27)$$

Rather than explicitly computing spatial derivatives of the velocity field, the second-order non-equilibrium

Hermite coefficient $a_{1,\alpha\beta}^{(2)}$ is approximated directly from the distribution functions as

$$a_{1,\alpha\beta}^{(2)} \approx \sum_i \mathcal{H}_{i,\alpha\beta}^{(2)} (f_i - f_i^{\text{eq}}). \quad (28)$$

It is worth noting that Eq. (24) is formally equivalent to

$$f_i^* = f_i^{\text{eq}} + (1 - \omega) f_i^{\text{neq,reg}}, \quad (29)$$

with

$$f_i^{\text{eq}} \equiv w_i \sum_{n=0}^4 \frac{1}{n! c_s^{2n}} \mathbf{a}_0^{(n)} : \mathcal{H}_i^{(n)}, \quad (30)$$

$$f_i^{\text{neq,reg}} \equiv w_i \sum_{n=0}^4 \frac{1}{n! c_s^{2n}} \mathbf{a}_1^{(n)} : \mathcal{H}_i^{(n)}. \quad (31)$$

Here, the former equilibrium contribution is given by Eq. (19), while the latter regularised non-equilibrium counterpart is

$$f_i^{\text{neq,reg}} \equiv w_i \sum_{n=0}^4 \frac{1}{n! c_s^{2n}} \mathbf{a}_1^{(n)} : \mathcal{H}_i^{(n)}, \quad (32)$$

which becomes

$$f_i^{\text{neq,reg}} = w_i \left[\frac{1}{2c_s^4} a_{1,\alpha\beta}^{(2)} \mathcal{H}_{i,\alpha\beta}^{(2)} + \frac{1}{6c_s^6} a_{1,\alpha\beta\gamma}^{(3)} \mathcal{H}_{i,\alpha\beta\gamma}^{(3)} + \frac{1}{24c_s^8} a_{1,\alpha\beta\gamma\delta}^{(4)} \mathcal{H}_{i,\alpha\beta\gamma\delta}^{(4)} \right]. \quad (33)$$

Algorithm of computation

Within a single time step, the proposed procedure executes the following six tasks at each grid point.

- Predict the macroscopic variables:

$$\rho = \sum_i f_i, \quad \mathbf{u} = \frac{\sum_i f_i \mathbf{c}_i}{\rho}, \quad \mathbf{b} = \sum_j \mathbf{g}_j.$$

- Evaluate the equilibrium populations:

$$\begin{aligned} f_i^{\text{eq}} &= w_i \rho \left[1 + \frac{\mathcal{H}_i^{(1)} \cdot \mathbf{u}}{c_s^2} + \frac{1}{2c_s^4} \mathcal{H}_i^{(2)} : \mathbf{u} \mathbf{u} + \right. \\ &\quad \left. \frac{1}{2c_s^6} (\mathcal{H}_{i,xxy}^{(3)} u_x^2 u_y + \mathcal{H}_{i,xyy}^{(3)} u_x u_y^2) + \right. \\ &\quad \left. \mathcal{H}_{i,xxyy}^{(4)} u_x^2 u_y^2 \right] + \\ &\quad \frac{w_i}{2c_s^4} \left[\frac{1}{2} |\mathbf{b}|^2 |\mathbf{c}_i|^2 - (\mathbf{c}_i \cdot \mathbf{b})^2 \right], \end{aligned}$$

$$g_{j,\alpha}^{\text{eq}} = \psi_j \left[b_\alpha + \frac{e_{j,\beta}}{c_s^2} (u_\beta b_\alpha - u_\alpha b_\beta) \right].$$

- Compute the non-equilibrium Hermite coefficients:

$$\begin{aligned} a_{1,\alpha\beta}^{(2)} &= \sum_i \mathcal{H}_{i,\alpha\beta}^{(2)} (f_i - f_i^{\text{eq}}), \\ a_{1,\alpha\beta\gamma}^{(3)} &= u_\alpha a_{1,\beta\gamma}^{(2)} + u_\beta a_{1,\alpha\gamma}^{(2)} + u_\gamma a_{1,\alpha\beta}^{(2)}, \\ a_{1,\alpha\beta\gamma\delta}^{(4)} &= u_\alpha a_{1,\beta\gamma\delta}^{(3)} + u_\beta a_{1,\alpha\gamma\delta}^{(3)} + u_\gamma a_{1,\alpha\beta\delta}^{(3)} + u_\delta a_{1,\alpha\beta\gamma}^{(3)} - \\ &\quad [u_\alpha u_\beta a_{1,\gamma\delta}^{(2)} + u_\alpha u_\gamma a_{1,\beta\delta}^{(2)} + u_\alpha u_\delta a_{1,\beta\gamma}^{(2)} + \\ &\quad u_\beta u_\gamma a_{1,\alpha\delta}^{(2)} + u_\beta u_\delta a_{1,\alpha\gamma}^{(2)} + u_\gamma u_\delta a_{1,\alpha\beta}^{(2)}]. \end{aligned}$$

- Reconstruct the non-equilibrium regularised populations:

$$\begin{aligned} f_i^{\text{neq,reg}} &= w_i \left[\frac{1}{2c_s^4} a_{1,\alpha\beta}^{(2)} \mathcal{H}_{i,\alpha\beta}^{(2)} + \frac{1}{6c_s^6} a_{1,\alpha\beta\gamma}^{(3)} \mathcal{H}_{i,\alpha\beta\gamma}^{(3)} + \right. \\ &\quad \left. \frac{1}{24c_s^8} a_{1,\alpha\beta\gamma\delta}^{(4)} \mathcal{H}_{i,\alpha\beta\gamma\delta}^{(4)} \right]. \end{aligned}$$

5. Perform the collision step:

$$\begin{aligned} f_i^* &= f_i^{\text{eq}} + (1 - \omega) f_i^{\text{neq,req}}, \\ \mathbf{g}_j^* &= \mathbf{g}_j^{\text{eq}} + (1 - \omega_m) (\mathbf{g}_j - \mathbf{g}_j^{\text{eq}}). \end{aligned}$$

6. Stream by

$$\begin{aligned} f_i(\mathbf{x} + \mathbf{c}_i \Delta t, t + \Delta t) &= f_i^*(\mathbf{x}, t), \\ \mathbf{g}_j(\mathbf{x} + \mathbf{e}_j \Delta t, t + \Delta t) &= \mathbf{g}_j^*(\mathbf{x}, t), \end{aligned}$$

and advance in time.

It is worth noting that the streaming step is implemented using the *swap* technique proposed by Latt²⁷, which enables the storage of only a single copy of the particle distribution functions. The interested reader is referred to the works of Geier & Schönherr²⁹ and Lehmann³⁰ for more recent approaches that likewise achieve single-population storage while preserving computational efficiency.

III. ORSZAG-TANG VORTEX

We assess the proposed recursive regularised formulation using the two-dimensional Orszag-Tang vortex, a canonical benchmark for non-linear MHD dynamics that exhibits rapid current-sheet formation and a subsequent transition toward MHD turbulence²⁶.

The initial velocity and magnetic fields are prescribed as

$$\begin{aligned} \mathbf{u}(\mathbf{x}, t=0) &= u_0 [-\sin(y), \sin(x)], \\ \mathbf{b}(\mathbf{x}, t=0) &= b_0 [-\sin(y), \sin(2x)], \end{aligned} \quad (34)$$

which satisfy the solenoidal constraints $\nabla \cdot \mathbf{u} = 0$ and $\nabla \cdot \mathbf{b} = 0$ by construction. The fluid mass density is initialised uniformly as $\rho_0 = 1$. All simulations are performed in a doubly periodic square domain $\Omega = [0, 2\pi] \times [0, 2\pi]$, discretised using a uniform Cartesian grid of $N \times N$ lattice nodes. The flow is characterised by the Reynolds and magnetic Prandtl numbers, with the former being defined as

$$\text{Re} = \frac{u_0 L}{\nu}, \quad (35)$$

where $L = 2\pi$ denotes the characteristic length scale, ν is the kinematic viscosity, and $u_0 = b_0 = 2$ being the root-mean-square of the fields in Eqs. (34). The Mach number of our simulations is set to $\text{Ma} = \tilde{u}_0/c_s \simeq 0.009$, where $\tilde{u}_0 = 0.2\pi^{-1}$ is the reference velocity expressed in lattice units. This value is sufficiently small to suppress spurious compressibility effects in the solution of the lattice Boltzmann equations. The choice of \tilde{u}_0 as a multiple of π^{-1} further facilitates sampling of flow quantities at salient discrete time steps.

Spatial derivatives are consistently evaluated using the isotropic lattice gradient

$$\partial_\alpha u_\beta(\mathbf{x}) = c_s^{-2} \sum_i [w_i u_\beta(\mathbf{x} + \mathbf{c}_i) c_{i,\alpha}],$$

$$\partial_\alpha b_\beta(\mathbf{x}) = c_s^{-2} \sum_i [w_i b_\beta(\mathbf{x} + \mathbf{c}_i) c_{i,\alpha}], \quad (36)$$

which is fully consistent with the underlying lattice symmetry³¹⁻³³.

We first consider a low-Reynolds-number configuration and benchmark our results against the spectral reference solution of Ref.¹⁰, as well as against three alternative lattice Boltzmann collision operators, the BGK, raw-moments-based, and central-moments-based formulations, which all employ fourth-order truncated equilibria for f_i in order to ensure a fair assessment. We then extend the analysis to turbulent regimes. Eventually, the computational cost involved by the present procedure is discussed.

A. Low-Reynolds-number flow

Following Orszag & Tang²⁶ and Dellar¹⁰, we consider the case $\text{Re} = 200\pi$ and monitor the temporal evolution of the peak electric current density, $j_{\max} = \max_\Omega |j_z|$, and peak vorticity, $\omega_{\max} = \max_\Omega |\omega_z|$, where j_z is evaluated from Eq. (22) and $\omega_z = \nabla \times \mathbf{u} = \partial_x u_y - \partial_y u_x$ by finite differences. All simulations employ identical physical parameters and initial conditions in order to isolate the effect of the collision operator. The magnetic Prandtl number is fixed to unity.

Tables I and II report the values of j_{\max} and ω_{\max} at representative times across progressively refined grids, together with the spectral reference solution.

At early times ($t = 0.5$), the flow remains smooth and well resolved. In this regime, all lattice Boltzmann formulations exhibit excellent agreement with the reference data. For the current density, the relative error is approximately 1.5% at $N = 128$ and decreases monotonically to 0.66% at $N = 512$ for all schemes. Similarly, for the vorticity, the finest-grid error drops below 5×10^{-4} , indicating that when gradients are mild the choice of collision model has negligible influence on accuracy.

As the system evolves toward $t = 1.0$, sharp magnetic gradients and emerging current sheets substantially increase the numerical stiffness of the problem. On the coarsest grid ($N = 128$), all LBMs underpredict both extrema. The BGK scheme yields slightly smaller discrepancies, with relative differences of 3.94% for j_{\max} and 10.09% for ω_{\max} , while the recursive regularised model displays marginally higher dissipation, reaching 4.23% and 10.95%, respectively. This behaviour indicates that regularisation introduces a modest additional damping of under-resolved non-equilibrium contributions.

Importantly, these differences vanish rapidly under grid refinement. At $N = 512$, all collision models converge toward the spectral reference with relative discrepancies of approximately 1.3% for j_{\max} and 1.4% for ω_{\max} . This confirms that while recursive regularisation is slightly more dissipative on coarse

meshes, it remains fully consistent with the reference solution and accurately captures the late-time nonlinear dynamics once sufficient resolution is provided.

| t | N | Ref. ¹⁰ | BGK | RMs | CMs | RR |
|-----|-----|--------------------|-------|-------|-------|-------|
| 0.5 | 128 | 17.96 | 17.69 | 17.69 | 17.69 | 17.69 |
| | 256 | 18.20 | 17.98 | 17.98 | 17.98 | 17.98 |
| | 512 | 18.24 | 18.12 | 18.12 | 18.12 | 18.12 |
| 1.0 | 128 | 45.13 | 43.35 | 43.25 | 43.24 | 43.22 |
| | 256 | 46.30 | 45.21 | 45.19 | 45.19 | 45.19 |
| | 512 | 46.59 | 45.98 | 45.98 | 45.97 | 45.97 |

TABLE I. Low-Reynolds-number flow: maximum current density j_{\max} at times $t = 0.5$ and $t = 1.0$, computed on progressively refined grids. Results obtained with different collision models are compared against a spectral reference solution.

| t | N | Ref. ¹⁰ | BGK | RMs | CMs | RR |
|-----|-----|--------------------|-------|-------|-------|-------|
| 0.5 | 128 | 6.744 | 6.670 | 6.666 | 6.666 | 6.670 |
| | 256 | 6.754 | 6.737 | 6.734 | 6.735 | 6.737 |
| | 512 | 6.758 | 6.755 | 6.753 | 6.753 | 6.755 |
| 1.0 | 128 | 14.07 | 12.65 | 12.57 | 12.56 | 12.53 |
| | 256 | 14.16 | 13.65 | 13.64 | 13.64 | 13.61 |
| | 512 | 14.20 | 14.01 | 14.00 | 14.00 | 13.99 |

TABLE II. Low-Reynolds-number flow: maximum vorticity ω_{\max} at times $t = 0.5$ and $t = 1.0$, computed on progressively refined grids. Results obtained with different collision models are compared against a spectral reference solution.

The preservation of the solenoidal constraint, $\nabla \cdot \mathbf{b} = 0$, is essential for physical fidelity in MHD simulations. Table III reports the maximum magnetic-field divergence. At $t = 1.0$, the divergence decreases from approximately 4.6×10^{-1} at $N = 128$ to 4.0×10^{-2} at $N = 512$ for all lattice Boltzmann schemes. Notably, the LBM results remain slightly below the spectral reference values. The near-identical behaviour across collision models demonstrates that divergence control is primarily governed by the discrete magnetic-field representation rather than by the specific regularisation of non-equilibrium moments.

| t | N | Ref. ¹⁰ | BGK | RMs | CMs | RR |
|-----|-----|--------------------|--------|--------|--------|--------|
| 0.5 | 128 | 0.0939 | 0.0619 | 0.0620 | 0.0620 | 0.0620 |
| | 256 | 0.0246 | 0.0201 | 0.0201 | 0.0201 | 0.0201 |
| | 512 | 0.0062 | 0.0056 | 0.0056 | 0.0056 | 0.0056 |
| 1.0 | 128 | 0.5642 | 0.4623 | 0.4583 | 0.4584 | 0.4587 |
| | 256 | 0.1611 | 0.1513 | 0.1512 | 0.1512 | 0.1512 |
| | 512 | 0.0415 | 0.0402 | 0.0402 | 0.0402 | 0.0402 |

TABLE III. Low-Reynolds-number flow: maximum magnetic-field divergence $\max_{\Omega} |\nabla \cdot \mathbf{b}|$ at times $t = 0.5$ and $t = 1.0$, computed on progressively refined grids. Results obtained with different collision models are compared against a spectral reference solution.

The sequence shown in Fig. 1 illustrates the temporal

evolution of the magnetic field obtained by our present RR procedure. Initially, the field retains the smooth, large-scale structure imposed by the initial condition, with well-organised alternating regions of magnetic intensity. As non-linear coupling intensifies, magnetic field lines undergo progressive stretching and folding, leading to the formation of thin filaments and elongated gradients. These structures correspond to the emergence of current sheets aligned with evolving shear layers, signalling the onset of magnetic reconnection. At later times, the magnetic topology becomes increasingly intermittent and complex, accompanied by a breakdown of the initial symmetries. This evolution directly underlies the growth of j_{\max} and ω_{\max} observed in the tables and reflects the transition toward fully non-linear MHD dynamics. Moreover, it corroborates the observations previously obtained by other collision operators ^{10,13,18,34}.

B. Turbulent regimes

We next investigate strongly non-linear regimes corresponding to $Re = 2500$ and 5000 . Tables IV–VII report the evolution of the peak current density and vorticity across progressively refined grids. These quantities directly probe the formation of thin current sheets and intense shear layers associated with magnetic reconnection and the ensuing turbulent cascade.

At early time ($t = 0.5$), the flow remains smooth and weakly non-linear. All collision models yield indistinguishable results and exhibit rapid grid convergence. For instance, at $Re = 2500$, variations in j_{\max} between $N = 500$ and $N = 2000$ remain below 1%, indicating that modest resolutions are sufficient prior to current-sheet formation.

As reconnection develops ($t \gtrsim 1$), sharp gradients emerge and the standard BGK formulation becomes unstable on coarse grids, systematically failing as current concentrations intensify. This breakdown coincides with the onset of thin current sheets and strong vortex roll-up, highlighting the inability of the BGK operator to control high-order non-equilibrium moments in severely under-resolved regimes. In contrast, all regularised and moment-based schemes remain fully stable throughout the evolution. Between $N = 1000$ and $N = 2000$, relative variations remain below 3×10^{-3} for j_{\max} and below 5×10^{-3} for ω_{\max} at all times, demonstrating very good grid convergence even in strongly turbulent conditions.

Interestingly, the monotonic growth of j_{\max} up to $t \approx 1$ reflects the progressive thinning of current sheets as magnetic field lines collapse and intensify. The subsequent decrease corresponds to reconnection events that release magnetic energy and promote turbulent mixing. Simultaneously, the growth of ω_{\max} indicates strong vortex stretching around reconnecting structures, confirming the tight coupling between

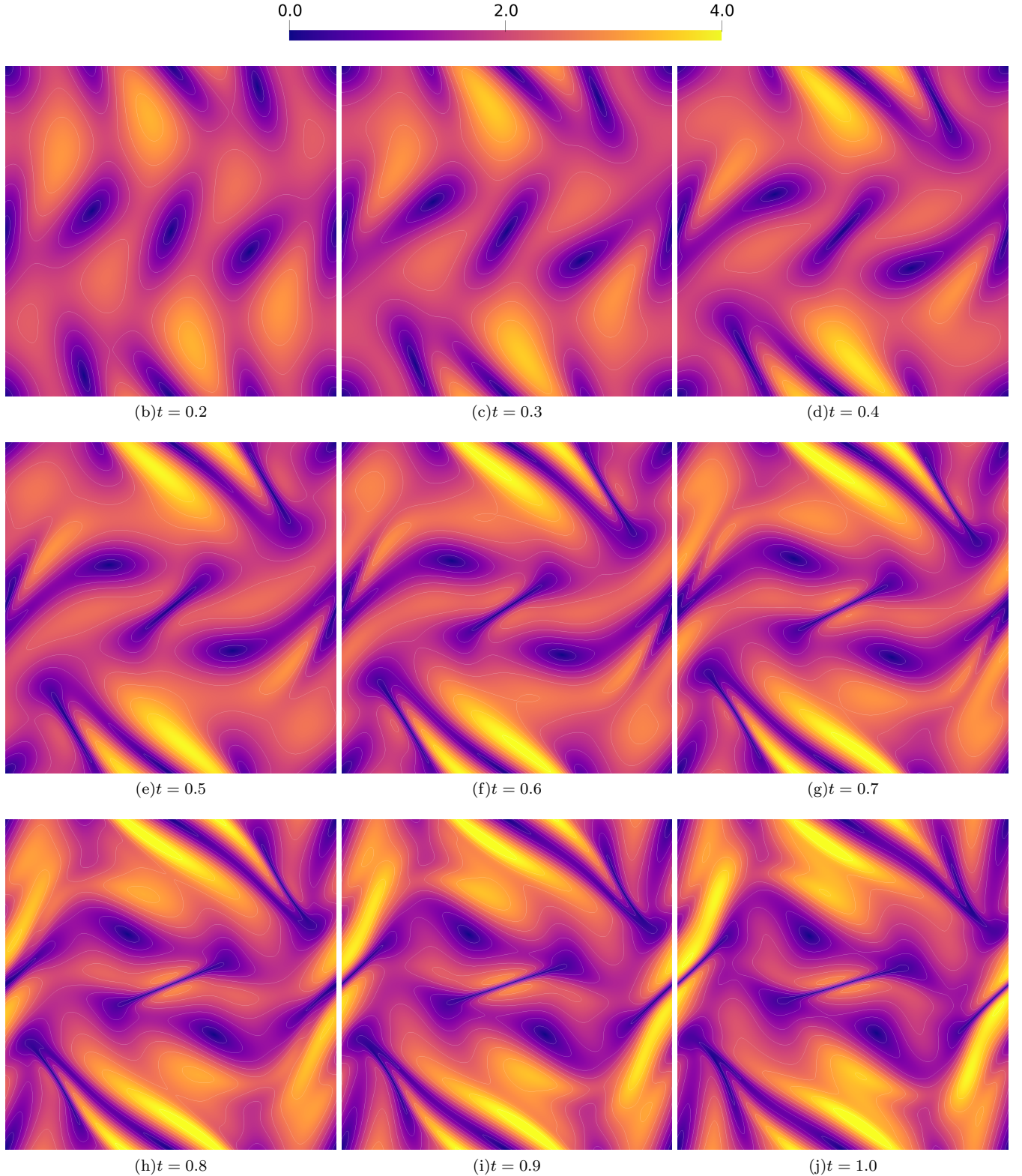


FIG. 1. Low-Reynolds-number flow: evolution of the magnetic field at selected time instants obtained by the RR LBM. The sequence illustrates the progressive distortion of the initial large-scale structures, the formation of thin current sheets, and the emergence of a highly intermittent magnetic field as the flow transitions toward fully non-linear MHD dynamics.

magnetic reconnection and shear-layer formation that drives the turbulent cascade.

Across both turbulent regimes, the recursive regularisation consistently reproduces the converged extrema with accuracy comparable to moment-based formulations while preserving stability even on the coarsest grids. This demonstrates that recursive filtering of non-equilibrium moments is sufficient to control under-resolved dynamics and accurately capture reconnection-driven intermittency, without requiring explicit moment reconstruction.

| t | N | BGK | RMs | CMs | RR |
|-----|------|--------|--------|--------|--------|
| 0.5 | 500 | 22.68 | 22.67 | 22.67 | 22.68 |
| | 1000 | 22.82 | 22.83 | 22.83 | 22.83 |
| | 2000 | 22.90 | 22.90 | 22.90 | 22.90 |
| 1.0 | 500 | Fail | 111.46 | 111.46 | 111.48 |
| | 1000 | 111.40 | 111.40 | 111.40 | 111.41 |
| | 2000 | 111.37 | 111.38 | 111.38 | 111.38 |
| 1.5 | 500 | Fail | 94.75 | 94.75 | 94.75 |
| | 1000 | 94.43 | 94.44 | 94.44 | 94.44 |
| | 2000 | 94.36 | 94.37 | 94.37 | 94.37 |
| 2.0 | 500 | Fail | 82.61 | 82.61 | 82.55 |
| | 1000 | 82.41 | 82.45 | 82.45 | 82.42 |
| | 2000 | 82.37 | 82.38 | 82.38 | 82.37 |
| 2.5 | 500 | Fail | 49.97 | 49.97 | 49.96 |
| | 1000 | 50.33 | 50.33 | 50.33 | 50.33 |
| | 2000 | 50.41 | 50.41 | 50.41 | 50.41 |
| 3.0 | 500 | Fail | 66.20 | 66.20 | 66.19 |
| | 1000 | 66.08 | 66.09 | 66.09 | 66.08 |
| | 2000 | 66.02 | 66.03 | 66.03 | 66.03 |
| 3.5 | 500 | Fail | 61.57 | 61.57 | 61.53 |
| | 1000 | 62.26 | 62.27 | 62.27 | 62.26 |
| | 2000 | 62.11 | 62.12 | 62.12 | 62.11 |
| 4.0 | 500 | Fail | 58.56 | 58.55 | 58.61 |
| | 1000 | 58.64 | 58.64 | 58.64 | 58.65 |
| | 2000 | 58.56 | 58.58 | 58.58 | 58.57 |

TABLE IV. $\text{Re} = 2500$: maximum current density j_{\max} at representative time instants, computed on progressively refined grids.

Fig. 2 depicts the temporal evolution of the magnetic field magnitude in the Orszag–Tang vortex at $\text{Re} = 500$, revealing the progressive development of MHD turbulence through field line stretching, sheet formation, and topological rearrangement.

At early times ($t = 0.5\text{--}1.0$), the magnetic structures remain smooth and large-scale, closely following the organised vortex pattern imposed by the initial condition. As non-linear coupling between the velocity and magnetic fields intensifies ($t = 1.5\text{--}2.0$), the magnetic field undergoes strong elongation and folding, leading to the formation of narrow regions of enhanced gradients. These localised structures mark the onset of current sheet formation, where magnetic energy is concentrated and dissipative processes become increasingly relevant.

In the later stages ($t = 2.5\text{--}4.0$), the flow transitions toward a fully developed turbulent regime characterized by thin, intermittent magnetic filaments and sheet-like

| t | N | BGK | RMs | CMs | RR |
|-----|------|-------|-------|-------|-------|
| 0.5 | 500 | 7.408 | 7.408 | 7.408 | 7.408 |
| | 1000 | 7.561 | 7.561 | 7.561 | 7.561 |
| | 2000 | 7.652 | 7.652 | 7.652 | 7.652 |
| 1.0 | 500 | Fail | 33.58 | 33.44 | 33.44 |
| | 1000 | 34.79 | 34.78 | 34.80 | 34.78 |
| | 2000 | 35.18 | 35.18 | 35.19 | 35.18 |
| 1.5 | 500 | Fail | 31.06 | 31.01 | 31.02 |
| | 1000 | 31.93 | 31.92 | 31.91 | 31.92 |
| | 2000 | 32.14 | 32.13 | 32.13 | 32.13 |
| 2.0 | 500 | Fail | 36.42 | 36.28 | 36.32 |
| | 1000 | 37.44 | 37.44 | 37.43 | 37.46 |
| | 2000 | 37.69 | 37.68 | 37.68 | 37.69 |
| 2.5 | 500 | Fail | 26.13 | 26.13 | 26.15 |
| | 1000 | 26.97 | 26.96 | 26.96 | 26.97 |
| | 2000 | 27.21 | 27.21 | 27.21 | 27.21 |
| 3.0 | 500 | Fail | 27.70 | 27.70 | 27.66 |
| | 1000 | 28.44 | 28.45 | 28.45 | 28.43 |
| | 2000 | 28.65 | 28.66 | 28.66 | 28.65 |
| 3.5 | 500 | Fail | 27.66 | 27.65 | 27.64 |
| | 1000 | 28.27 | 28.28 | 28.28 | 28.28 |
| | 2000 | 28.38 | 28.39 | 28.38 | 28.38 |
| 4.0 | 500 | Fail | 25.30 | 25.29 | 25.25 |
| | 1000 | 25.92 | 25.93 | 25.93 | 25.91 |
| | 2000 | 26.10 | 26.11 | 26.11 | 26.10 |

TABLE V. $\text{Re} = 2500$: maximum vorticity ω_{\max} at representative time instants, computed on progressively refined grids.

| t | N | BGK | RMs | CMs | RR |
|-----|------|--------|--------|--------|--------|
| 0.5 | 500 | Fail | 23.71 | 23.71 | 23.72 |
| | 1000 | 469.97 | 23.90 | 23.90 | 23.90 |
| | 2000 | 23.98 | 23.98 | 23.98 | 23.98 |
| 1.0 | 500 | Fail | 168.97 | 169.00 | 169.06 |
| | 1000 | Fail | 169.66 | 169.66 | 169.69 |
| | 2000 | 169.67 | 169.67 | 169.67 | 169.69 |
| 1.5 | 500 | Fail | 144.32 | 144.31 | 144.32 |
| | 1000 | Fail | 142.95 | 142.95 | 142.96 |
| | 2000 | 142.53 | 142.54 | 142.54 | 142.55 |
| 2.0 | 500 | Fail | 131.43 | 131.4 | 131.33 |
| | 1000 | Fail | 131.53 | 131.52 | 131.49 |
| | 2000 | 131.42 | 131.45 | 131.45 | 131.43 |
| 2.5 | 500 | Fail | 93.58 | 93.58 | 93.60 |
| | 1000 | Fail | 93.41 | 93.41 | 93.45 |
| | 2000 | 92.94 | 92.92 | 92.92 | 92.94 |
| 3.0 | 500 | Fail | 79.32 | 79.26 | 79.96 |
| | 1000 | Fail | 76.10 | 76.09 | 76.50 |
| | 2000 | 75.58 | 75.58 | 75.58 | 75.59 |
| 3.5 | 500 | Fail | 201.32 | 201.62 | 202.14 |
| | 1000 | Fail | 190.36 | 190.36 | 193.03 |
| | 2000 | 180.12 | 180.15 | 180.15 | 182.47 |
| 4.0 | 500 | Fail | 129.37 | 129.33 | 129.22 |
| | 1000 | Fail | 130.67 | 130.66 | 130.53 |
| | 2000 | 130.99 | 131.04 | 131.03 | 130.94 |

TABLE VI. $\text{Re} = 5000$: maximum current density j_{\max} at representative time instants, computed on progressively refined grids.

| t | N | BGK | RM | CM | RR |
|-----|------|---------|-------|-------|-------|
| 0.5 | 500 | Fail | 7.698 | 7.698 | 7.697 |
| | 1000 | 46.2653 | 7.808 | 7.808 | 7.807 |
| | 2000 | 7.886 | 7.886 | 7.886 | 7.886 |
| 1.0 | 500 | Fail | 49.65 | 48.96 | 48.98 |
| | 1000 | Fail | 51.75 | 51.64 | 51.60 |
| | 2000 | 52.61 | 52.61 | 52.62 | 52.60 |
| 1.5 | 500 | Fail | 47.49 | 47.49 | 47.28 |
| | 1000 | Fail | 49.31 | 49.27 | 49.27 |
| | 2000 | 49.82 | 49.80 | 49.79 | 49.80 |
| 2.0 | 500 | Fail | 57.69 | 56.85 | 57.01 |
| | 1000 | Fail | 60.54 | 60.41 | 60.45 |
| | 2000 | 61.13 | 61.13 | 61.12 | 61.14 |
| 2.5 | 500 | Fail | 45.88 | 45.82 | 45.52 |
| | 1000 | Fail | 47.57 | 47.56 | 47.39 |
| | 2000 | 47.99 | 48.01 | 48.01 | 47.92 |
| 3.0 | 500 | Fail | 45.35 | 45.41 | 45.38 |
| | 1000 | Fail | 47.16 | 47.17 | 47.11 |
| | 2000 | 47.51 | 47.51 | 47.52 | 47.47 |
| 3.5 | 500 | Fail | 66.72 | 66.45 | 65.90 |
| | 1000 | Fail | 74.40 | 74.40 | 74.90 |
| | 2000 | 75.34 | 75.33 | 75.34 | 75.84 |
| 4.0 | 500 | Fail | 49.42 | 49.32 | 49.82 |
| | 1000 | Fail | 53.50 | 53.48 | 53.76 |
| | 2000 | 54.51 | 54.53 | 54.53 | 54.67 |

TABLE VII. $Re = 5000$: maximum vorticity ω_{\max} at representative time instants, computed on progressively refined grids.

structures distributed throughout the domain. Such features are classical signatures of magnetic reconnection events, whereby distorted field lines rapidly change topology and release stored magnetic energy across multiple scales. The coexistence of intense localised structures with broader turbulent patterns reflects the underlying cascade of magnetic energy from large to small scales.

The accurate capture of sharp current sheets and reconnection-driven dynamics without spurious oscillations or excessive diffusion highlights the robustness of the present formulation in resolving multiscale MHD phenomena at high Reynolds numbers.

Synthesis across flow regimes

Taken together, the low-Reynolds-number and turbulent results provide a coherent picture of the role of non-equilibrium control in MHD lattice Boltzmann models. In mildly non-linear regimes dominated by smooth structures, all collision operators perform equivalently, confirming that regularisation does not degrade accuracy in resolved flows. As the dynamics transition toward strongly non-linear behaviour characterised by thin current sheets, magnetic reconnection, and intense shear layers, the numerical challenge shifts from accuracy to stability and robustness.

In this regime, the failure of the BGK scheme contrasts sharply with the sustained convergence of more sophisticated formulations. Recursive regularisation emerges as a strategy that preserves accuracy in laminar conditions while ensuring stability in turbulent MHD flows, enabling reliable simulation across the full spectrum of reconnection-driven dynamics encountered in the Orszag–Tang vortex.

Fig. 3 reports the temporal evolution of the maximum electric current density. This quantity directly probes the formation and intensification of current sheets and therefore provides a sensitive measure of magnetic reconnection and non-linear MHD activity. At early times ($t \lesssim 0.5$), all curves collapse closely, indicating that the flow remains smooth and weakly non-linear, with magnetic gradients growing in a similar manner regardless of Reynolds number. During this phase, current amplification is dominated by large-scale field-line stretching imposed by the initial vortex configuration. As the system evolves toward $t \approx 1$, a rapid increase in j_{\max} is observed, corresponding to the progressive thinning of current sheets and the onset of reconnection. This growth becomes increasingly pronounced with Reynolds number. While the low-Re case exhibits a relatively mild peak, both turbulent regimes display substantially stronger current intensification, reflecting reduced dissipation and sharper magnetic gradients. The ordering $j_{\max}(Re = 5000) > j_{\max}(Re = 2500) \gg j_{\max}(Re = 200\pi)$ highlights the enhanced collapse of current layers as inertial effects dominate over resistive smoothing. Beyond the peak, j_{\max} decreases as reconnection events release magnetic energy and promote topological reorganisation of the field. This decay is more gradual and occurs at higher levels in the turbulent regimes, consistent with sustained intermittency and the continuous formation of secondary current sheets characteristic of fully developed MHD turbulence. In contrast, the low-Re flow rapidly relaxes toward a smoother state with significantly weaker magnetic gradients.

The energy evolution further clarifies the role of current-sheet dynamics in driving the non-linear MHD transition. The averaged kinetic and magnetic energies of the system are defined as

$$E_k = \frac{1}{2L^2} \int_{\Omega} |\mathbf{u}|^2 d\Omega, \quad E_m = \frac{1}{2L^2} \int_{\Omega} |\mathbf{b}|^2 d\Omega, \quad (37)$$

respectively. In all cases, the initial phase is characterised by a gradual amplification of magnetic energy through large-scale field-line stretching, while kinetic energy remains comparatively weak. As the system approaches the time of peak current density (see Fig. 4), a rapid drop in magnetic energy is observed simultaneously with a sharp rise in kinetic energy, indicating efficient conversion of magnetic energy into flow motion through reconnection events occurring within the thinned current sheets. This transfer becomes increasingly pronounced with Reynolds number: the

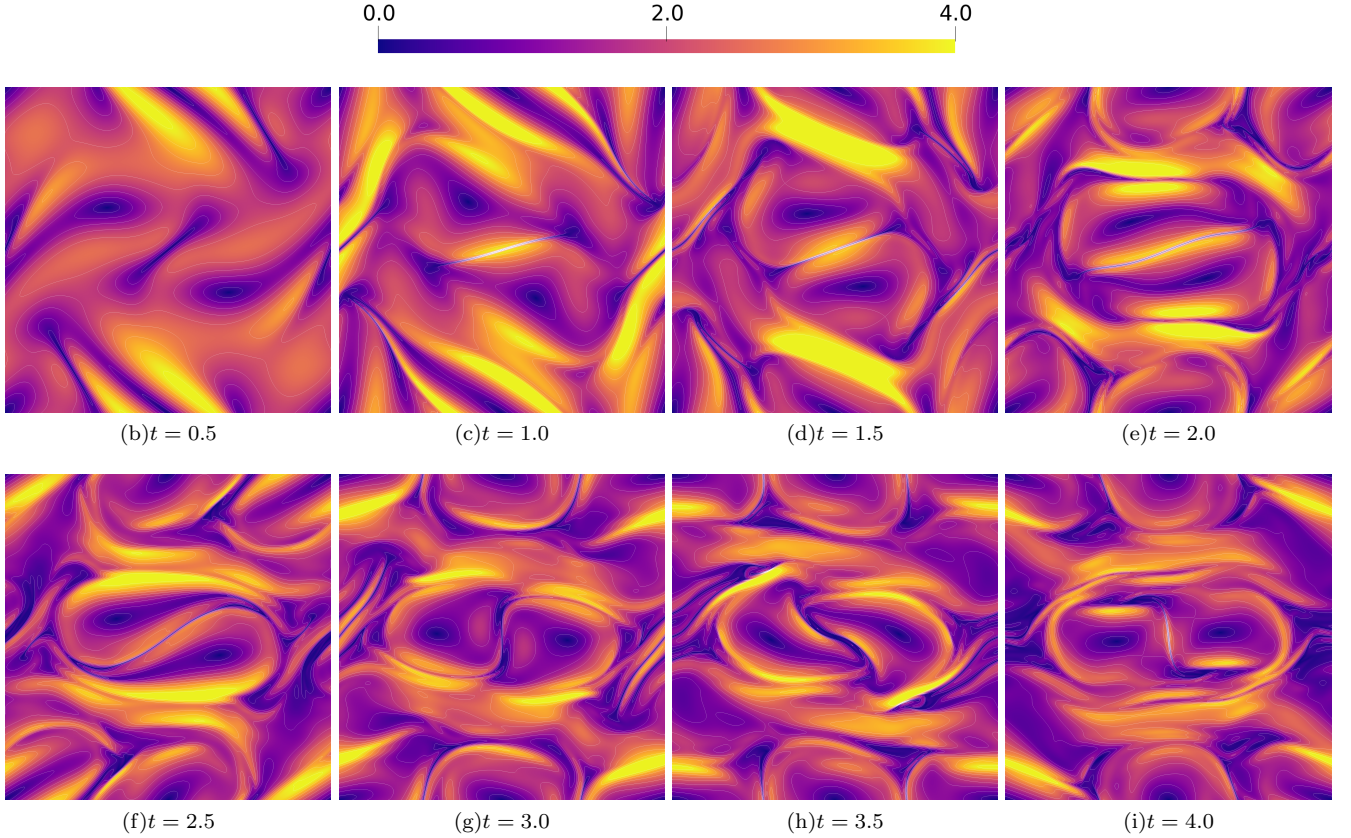


FIG. 2. $\text{Re} = 5000$: evolution of the magnetic field at selected time instants. Snapshots illustrate the transition from large-scale coherent structures to fully developed turbulent magnetic filaments.

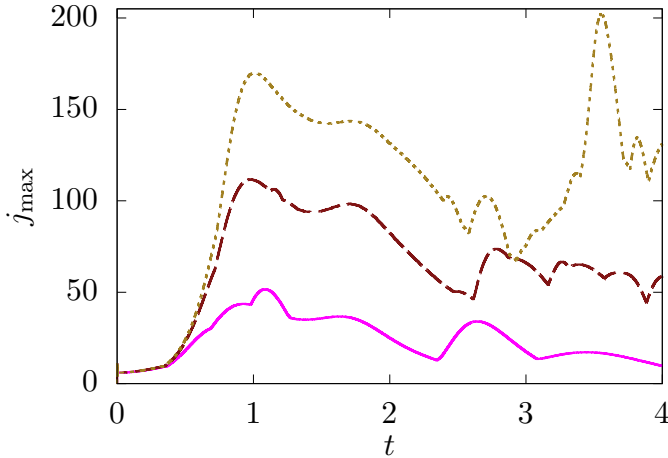


FIG. 3. Temporal evolution of the peak electric current density $j_{\max} = \max_{\Omega} |j_z|$ for the Orszag–Tang vortex at $\text{Re} = 200\pi$ (magenta solid line), $\text{Re} = 2500$ (brown dashed line), and $\text{Re} = 5000$ (olive line with smaller dashes). The initial growth reflects large-scale magnetic field-line stretching, followed by a rapid intensification associated with current-sheet thinning and the onset of magnetic reconnection. Increasing Reynolds number leads to stronger current concentration and sustained intermittency, characteristic of turbulent MHD dynamics. Findings are obtained by the present RR scheme.

turbulent regimes exhibit stronger magnetic energy depletion and enhanced kinetic energisation, consistent with the higher j_{\max} values associated with more intense current-sheet collapse. Following the reconnection burst, both energies approach a slowly decaying, fluctuating state, reflecting sustained turbulent mixing and the continuous formation of secondary current sheets. In contrast, the low-Reynolds-number case rapidly relaxes toward a smoother configuration with significantly weaker energy exchange, in agreement with its lower peak current intensification.

C. Computational cost

We conclude the performance assessment of the lattice Boltzmann formulations for MHD with an evaluation of their computational cost. Fig. 5 summarises the normalised runtime of the four lattice Boltzmann models as a function of the total number of grid points, N^2 . Analyses are carried out by varying $N \in [200 : 2000]$. While all approaches perform within a similar order of magnitude, clear and systematic differences emerge in the absolute runtime, reflecting the distinct algebraic complexity of the underlying collision operators.

Across the entire range of resolutions considered, the

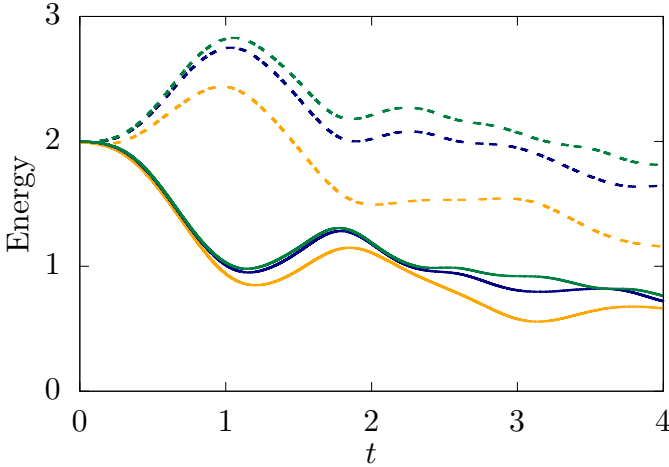


FIG. 4. Time evolution of kinetic (solid lines) and magnetic (dashed lines) energies for the Orszag–Tang vortex at $Re = 200\pi$ (orange), $Re = 2500$ (navy), and $Re = 5000$ (dark green). At early times, magnetic energy dominates as the initial field is stretched by the flow. As non-linear interactions intensify, magnetic energy is rapidly converted into kinetic energy through current-sheet formation and magnetic reconnection. Increasing Reynolds number leads to stronger energy transfer, delayed saturation, and enhanced turbulent mixing, with higher- Re cases exhibiting sustained kinetic activity and slower magnetic dissipation characteristic of fully developed MHD turbulence. Findings are obtained by the present RR scheme.

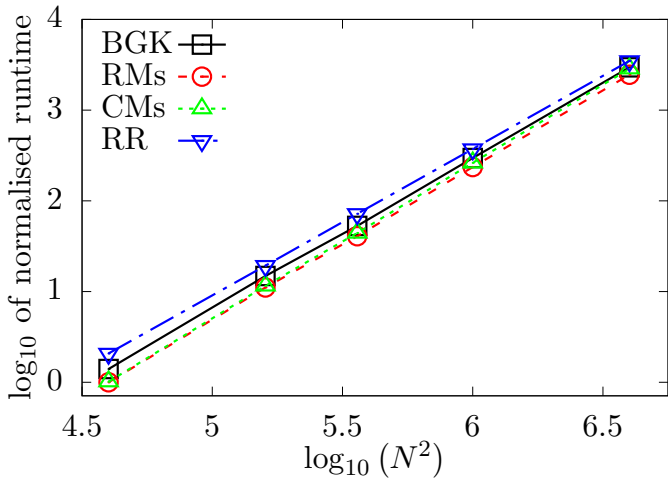


FIG. 5. Computational cost: normalised runtime as a function of N^2 for the BGK (solid black line with squares), RMs (dashed red line with circles), CMs (green dotted line with triangles), and RR (blue dash-dotted line with inverted triangles) schemes in log-log scale. Moments-based LBMs consistently provide the most efficient performance.

RR model displays the highest runtime. This behaviour is a direct consequence of the more elaborate collision step, which involves the projection of non-equilibrium populations onto Hermite polynomials followed by recursive reconstruction procedures. While these

operations improve numerical stability, they introduce a measurable computational overhead that persists as the problem size increases.

In contrast, the RMs and CMs formulations consistently define the lower bound of the runtime envelope. The near-perfect overlap of their curves in Fig. 5 indicates that the additional velocity-dependent shift required by the CMs approach incurs a negligible cost relative to the dominant streaming operations. This result confirms that relaxation in moment space can be achieved without sacrificing computational efficiency.

Despite its apparent algorithmic simplicity, the BGK model does not achieve the lowest runtime. As shown in Fig. 5, both the RMs and CMs models outperform BGK across all tested resolutions. This suggests that the moment-space formulation enables a more efficient evaluation of the collision operator, due to reduced floating-point operations in the equilibrium reconstruction compared with the direct population-based BGK relaxation.

We can conclude that moment-based collision operators provide a favourable balance between computational efficiency and modelling sophistication, while the RR approach trades increased runtime for enhanced numerical robustness.

IV. CONCLUSIONS

We have introduced and assessed a recursive regularised lattice Boltzmann method for two-dimensional incompressible magnetohydrodynamics. The proposed scheme retains the efficiency and locality of Dellar’s double-distribution framework for MHD, while enhancing the fluid solver through a Hermite-based recursive reconstruction of the non-equilibrium distribution. By combining a fourth-order Hermite equilibrium on D2Q9 with a regularised non-equilibrium built from physically consistent Hermite coefficients, the method selectively filters spurious lattice-supported kinetic contributions without requiring explicit velocity-gradient evaluations.

The Orszag–Tang vortex was used as a stringent benchmark to quantify accuracy, dissipation, and robustness against established collision models (BGK, raw-moment MRT, and central-moment formulations) under otherwise identical settings. In the well-resolved early evolution, all schemes closely match spectral reference data for peak current density and vorticity. As the flow develops sharp gradients and current sheets, the recursive regularisation introduces a modest additional dissipation on coarse grids, leading to slightly lower extrema compared with BGK. Importantly, this discrepancy diminishes under grid refinement: on the finest meshes, the RR results converge to the same level of agreement achieved by the competing collision operators, confirming consistency with the reference solution in the physically relevant regime.

We further examined the solenoidal constraint on the magnetic field. All tested lattice Boltzmann formulations display clear rapid decay of the maximum divergence error with increasing resolution, and the differences between collision models remain negligible. This indicates that the divergence behaviour is primarily controlled by the discrete magnetic-field representation (D2Q5) rather than by the regularisation of the fluid non-equilibrium moments. Qualitatively, the RR scheme reproduces the canonical Orszag–Tang dynamics, including the progressive distortion of large-scale magnetic structures, the formation of thin current sheets, and the emergence of intermittent filamentary features, in line with established MHD studies within the LBM community.

In turbulent regimes dominated by intermittent current sheets and reconnection-driven dynamics, recursive regularisation demonstrates robustness comparable to moment-based approaches while retaining the simplicity and efficiency of a single-relaxation-time framework. The accurate capture of peak current intensification, vorticity growth, and magnetic topology evolution confirms that the method preserves the essential physical mechanisms governing MHD turbulence.

From a computational standpoint, the recursive regularisation entails a moderate increase in per-time-step cost due to the additional Hermite projections and recursive reconstructions performed during the collision step. Nevertheless, the algorithm preserves the strictly local character of the lattice Boltzmann method and maintains linear scaling with system size. As a result, the added overhead remains controlled and does not compromise the favourable parallel efficiency or memory-access patterns of standard LBM formulations. In practical terms, the improved numerical robustness offered by the RR scheme can offset this additional cost by enabling stable simulations at coarser resolutions or under more demanding physical conditions.

In summary, our results demonstrate that recursive regularisation can be transferred to coupled MHD systems in a simple and systematic manner, delivering a robust stabilisation strategy while preserving the correct incompressible MHD limit. Beyond the benchmark considered here, the proposed formulation provides a practical route to regularised lattice Boltzmann solvers for broader multiphysics settings. Natural next steps include the extension to three-dimensional lattices^{35,36} and the development of consistent regularisation strategies for the magnetic populations to further reduce lattice artefacts at extreme transport parameters.

SUPPLEMENTAL MATERIAL

The supplemental material is available at <https://github.com/SIG-LBM-Multiphysics-Modelling/>

RecursiveRegularised_MHD. It includes all C++ programs used to reproduce the numerical simulations presented in this work. The implementations are written using the `Kokkos` library³⁷, ensuring performance portability across diverse hardware architectures.

ACKNOWLEDGMENTS

The author is grateful to Dr. Abinhav Muta for his help with the `Kokkos` library.

REFERENCES

- ¹D. Biskamp, *Magnetohydrodynamic Turbulence* (Cambridge University Press, 2003).
- ²P. A. Davidson and E. V. Belova, “An introduction to magnetohydrodynamics,” *American Journal of Physics* **70**, 781–781 (2002).
- ³P. Mininni, A. Pouquet, and D. Montgomery, “Small-scale structures in three-dimensional magnetohydrodynamic turbulence,” *Physical review letters* **97**, 244503 (2006).
- ⁴J. Fang, S. Laizet, and A. Skillen, “A high-order finite-difference solver for direct numerical simulations of magnetohydrodynamic turbulence,” *Computer Physics Communications* **307**, 109400 (2025).
- ⁵T. Krüger, H. Kusumaatmaja, A. Kuzmin, O. Shardt, G. Silva, and E. M. Viggen, *The Lattice Boltzmann Method: Principles and Practice* (Springer, 2016).
- ⁶D. Montgomery and G. D. Doolen, “Magnetohydrodynamic cellular automata,” *Physics Letters A* **120**, 229–231 (1987).
- ⁷S. Chen, H. Chen, D. Martnez, and W. Matthaeus, “Lattice Boltzmann model for simulation of magnetohydrodynamics,” *Physical Review Letters* **67**, 3776–3779 (1991).
- ⁸D. O. Martínez, S. Chen, and W. H. Matthaeus, “Lattice Boltzmann magnetohydrodynamics,” *Physics of Plasmas* **1**, 1850–1867 (1994).
- ⁹S. Succi, M. Vergassola, and R. Benzi, “Lattice Boltzmann scheme for two-dimensional magnetohydrodynamics,” *Physical Review A* **43**, 4521–4524 (1991).
- ¹⁰P. J. Dellar, “Lattice Boltzmann algorithms for magnetohydrodynamics,” *Journal of Computational Physics* **179**, 95–126 (2002).
- ¹¹P. L. Bhatnagar, E. P. Gross, and M. Krook, “A model for collision processes in gases. I. Small amplitude processes in charged and neutral one-component systems,” *Physical Review* **94**, 511–525 (1954).
- ¹²J. Latt and B. Chopard, “Lattice Boltzmann method with regularized pre-collision distribution functions,” *Mathematics and Computers in Simulation* **72**, 165–168 (2006).
- ¹³A. De Rosis, E. Lévéque, and R. Chahine, “Advanced lattice Boltzmann scheme for high-reynolds-number magneto-hydrodynamic flows,” *Journal of Turbulence* **19**, 446–462 (2018).
- ¹⁴P. Lallemand and L.-S. Luo, “Theory of the lattice Boltzmann method: Acoustic and thermal properties,” *Physical Review E* **61**, 6546–6562 (2000).
- ¹⁵D. d’Humières, “Multiple-relaxation-time lattice Boltzmann models in three dimensions,” *Philosophical Transactions of the Royal Society A: Mathematical, Physical and Engineering Sciences* **360**, 437–451 (2002).
- ¹⁶M. Geier, A. Greiner, and J. Korvink, “Cascaded digital lattice Boltzmann automata for high reynolds number flow,” *Physical Review E* **73**, 066705 (2006).

¹⁷M. Geier, M. Schönherr, A. Pasquali, and M. Krafczyk, “The cumulant lattice Boltzmann equation in three dimensions: Theory and validation,” *Computers & Mathematics with Applications* **70**, 507–547 (2015).

¹⁸A. De Rosis, “Nonorthogonal central-moments-based lattice Boltzmann scheme in three dimensions,” *Physical Review E* **95**, 013310 (2017).

¹⁹A. De Rosis, R. Huang, and C. Coreixas, “Universal formulation of central-moments-based lattice Boltzmann method with external forcing for the simulation of multiphysics phenomena,” *Physics of Fluids* **31**, 117102 (2019).

²⁰S. Patnaik, A. Skillen, and A. De Rosis, “Three-dimensional electrohydrodynamic flows by a central-moments-based lattice Boltzmann method,” *Engineering with Computers* **41**, 4977–5002 (2025).

²¹O. Malaspinas, “Increasing stability and accuracy of the lattice Boltzmann scheme: recursivity and regularization,” *arXiv preprint arXiv:1505.06900* (2015), 10.48550/arXiv.1505.06900.

²²C. Coreixas, G. Wissocq, B. Chopard, and J. Latt, “Recursive regularization step for high-order lattice Boltzmann methods,” *Physical Review E* **96**, 033306 (2017).

²³C. Coreixas *et al.*, “Impact of collision models on the physical properties and isotropy of lattice Boltzmann methods,” *Philosophical Transactions of the Royal Society A* **378**, 20190397 (2020).

²⁴J. Lu, T. Gregorczyk, S. Zhao, and P. Boivin, “Phase-field-based recursive regularized multiphase lattice Boltzmann model with a consistent pressure scheme,” *International Journal of Multiphase Flow* **195**, 105500 (2026).

²⁵Z. Xiong, L. Zhang, and S. Guo, “Numerical study of magnetohydrodynamics based on the recursive regularized lattice boltzmann method,” in *Proceedings of the 32nd International Conference on Nuclear Engineering—Volume 11; ICONE 2025, 22–26 June, Weihai, China*, edited by S. Tan, W. Xu, and Y. Zhu (Springer Nature Singapore, Singapore, 2026) pp. 457–467.

²⁶S. A. Orszag and C.-M. Tang, “Small-scale structure of two-dimensional magnetohydrodynamic turbulence,” *Journal of Fluid Mechanics* **90**, 129–143 (1979).

²⁷J. Latt, “Technical report: How to implement your DdQ_q dynamics with only q variables per node (instead of 2q),” *Tufts University*, 1–8 (2007).

²⁸M. Pattison, K. Premnath, N. Morley, and M. Abdou, “Progress in lattice Boltzmann methods for magnetohydrodynamic flows relevant to fusion applications,” *Fusion Engineering and Design* **83**, 557–572 (2008).

²⁹M. Geier and M. Schönherr, “Esoteric twist: An efficient in-place streaming algorithmus for the lattice Boltzmann method on massively parallel hardware,” *Computation* **5** (2017), 10.3390/computation5020019.

³⁰M. Lehmann, “Esoteric pull and esoteric push: Two simple in-place streaming schemes for the lattice Boltzmann method on gpus,” *Computation* **10** (2022), 10.3390/computation10060092.

³¹K. K. Mattila, L. A. Hegele Júnior, and P. C. Philippi, “High-accuracy approximation of high-rank derivatives: Isotropic finite differences based on lattice-Boltzmann stencils,” *The Scientific World Journal* **2014**, 142907 (2014).

³²S. Saito, Y. Abe, and K. Koyama, “Lattice Boltzmann modeling and simulation of liquid jet breakup,” *Physical Review E* **96**, 013317 (2017).

³³S. Saito, A. De Rosis, A. Festuccia, A. Kaneko, Y. Abe, and K. Koyama, “Color-gradient lattice Boltzmann model with nonorthogonal central moments: Hydrodynamic melt-jet breakup simulations,” *Physical Review E* **98**, 013305 (2018).

³⁴A. De Rosis, R. Liu, and A. Revell, “One-stage simplified lattice Boltzmann method for two- and three-dimensional magnetohydrodynamic flows,” *Physics of Fluids* **33**, 085114 (2021).

³⁵R. Foldes, E. Lévéque, R. Marino, E. Pietropaolo, A. De Rosis, D. Telloni, and F. Feraco, “Efficient kinetic lattice Boltzmann simulation of three-dimensional Hall-MHD turbulence,” *Journal of Plasma Physics* **89**, 905890413 (2023).

³⁶C. Vásconez, R. Foldes, R. Marino, R. Manobanda, E. Lévéque, D. Telloni, and L. Sorriso-Valvo, “A parametric study of the turbulent energy transfer in three-dimensional lattice-Boltzmann Hall-MHD plasma simulations,” *Physics of Plasmas* **33** (2026), 10.1063/5.0298970.

³⁷C. R. Trott, D. Lebrun-Grandié, D. Arndt, J. Ciesko, V. Dang, N. Ellingwood, R. Gayatri, E. Harvey, D. S. Hollman, D. Ibanez, N. Liber, J. Madsen, J. Miles, D. Poliakoff, A. Powell, S. Rajamanickam, M. Simberg, D. Sunderland, B. Turcksin, and J. Wilke, “Kokkos 3: Programming model extensions for the exascale era,” *IEEE Transactions on Parallel and Distributed Systems* **33**, 805–817 (2022).